

Optical Characterization of Strongly Correlated Magnetoresistive Manganite Film: $\text{La}_{0.67}\text{Ca}_{0.33}\text{MnO}_3$

Naween Anand, Naveen Margankunte,^{*} Hyoungeen Jeon,[†] Amlan Biswas, and D. B. Tanner

Department of Physics, University of Florida, Gainesville, FL 32611-8440, USA

(Dated: December 18, 2015)

Abstract

The focus on manganites has led experimentalists and theorists to better understand the behavior of electrons in a strongly correlated system. Reflectivity as a function of temperature has been measured for the manganite thin-film samples across the metal-insulator transition in this article. The optical properties in the infrared and visible range were determined by fits to a Drude-Lorentz model, using exact formulas for the thin film optics and the measured properties of the substrate. The phonon modes were identified and verified with lattice dynamical calculations for distorted orthorhombic crystal structure of the material. The reflectance has strong temperature dependence in the far infrared and in the region of the phonons, rising as the temperature is lowered and the film becomes metallic. Temperature dependence of phonon modes has been discussed after fitting the temperature dependent spectra using Drude-Lorentz model. In the near-infrared and visible range, there are midgap conductivity peaks due to electronic band transition showing shifting behavior with temperature change.^{1,2}

I. INTRODUCTION

Strongly correlated electron systems have been quite interesting but challenging field of active research in condensed matter physics since last few decades. The rich ground states which these materials exhibit result from unusual spin, charge, lattice and orbital degrees of freedom. Phase diagrams of numerous manganite families indicate that there is competition between various phases at the boundaries within the crystal which leads to intrinsically inhomogeneous systems. These manganites have been a potential candidates for non-volatile Magnetoresistive Random Access Memory (MRAM) modules due to an increased areal density. Thin films or single crystals of these manganites could also be used in making magnetic sensors, bolometric detectors and as a chemical catalyst in automobile industry. Besides, these manganites also possess ferroelectric properties making them conducive for non-volatile ferroelectric field effect device application.

The general chemical formula for this series of manganese oxides is $\text{RE}_{1-x}\text{A}_x\text{MnO}_3$ with RE^{3+} a rare earth trivalent cation and A^{2+} an alkaline divalent cation. Oxygen is in O^{2-} state, and the relative fraction of Mn^{4+} to Mn^{3+} is regulated by the composition x . The fundamental physical properties of hole doped LaMnO_3 , generically termed “manganites,” and much of the underlying physics were first described by Jonker and Santen in 1950.^{3,4} Several mixed polycrystalline manganite crystals such as $(\text{La}, \text{Ca})\text{MnO}_3$, $(\text{La}, \text{Sr})\text{MnO}_3$ and $(\text{La}, \text{Ba})\text{MnO}_3$ were prepared using standard ceramic technique. All these mixed crystals were found in perovskite structure which displayed ferromagnetic properties along with anomalies in the conductivity at the Curie temperature which itself was found strongly dependent on the extent of hole doping. This unusual correlation between magnetism and transport properties was explained by the author in terms of a novel concept termed a “double exchange” mechanism.⁵ In order to understand the behavior of the doped systems, the logical starting point is to get an insight of the undoped parent compounds. LaMnO_3 is an insulating paramagnetic material with orthorhombic crystal structure that orders antiferromagnetically at around 140 K. A-type ordering was reported by Wollan and Koehler in 1955 in their neutron diffraction studies in which the magnetic moments lie in the $a - c$ plane and possess ferromagnetic alignment along a -axis while successive planes along b -axis are aligned antiparallel. Similarly for CaMnO_3 , another orthorhombic insulating paramagnetic material, which goes to antiferromagnetic phase around 130-K. This is G-type ordering in which all moments are

aligned in antiferromagnetic order in all three directions.^{6,7}. Reported properties for these compounds, however, have varied rather dramatically both in terms of the crystal structure and magnetic ordering. There are various factors which control the chemical and magnetic structure of these compounds. Annealing in oxygen introduces small amount of oxygen in the system, which appears to be accommodated by La or Mn vacancies in the structure. Also the relative percentage amount of Mn^{4+} ion over Mn^{3+} ion in the system induces deviation from the undoped behavior. Raman studies on these materials also confirm the structural change in system depending on different synthesizing conditions.

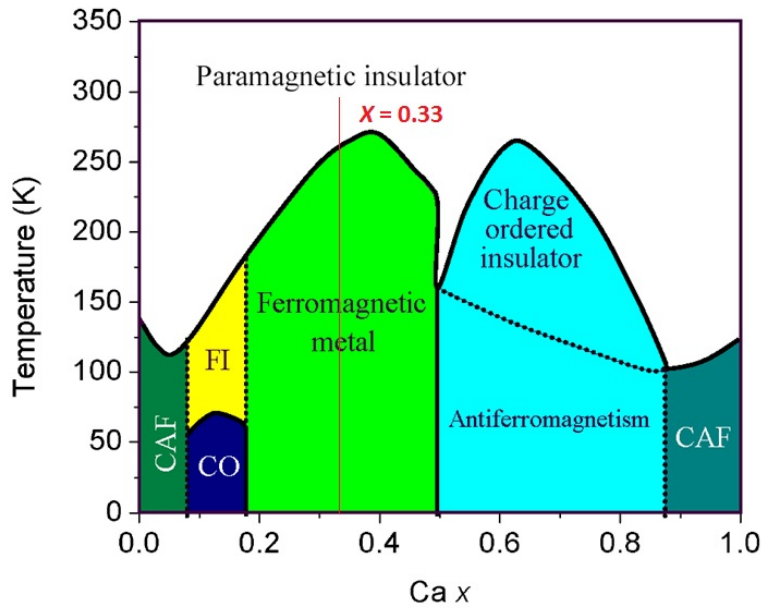


FIG. 1. (Color online) Phase diagram of $\text{La}_{1-x}\text{Ca}_x\text{MnO}_3$ doped manganite as a function of stoichiometric concentration x . Courtesy to Dr. Amlan Biswas for providing the figure.

Besides some early progress in the field of manganites, a strong upsurge in the research interest came about after the remarkable discovery of the colossal magnetoresistance (CMR) effect in 1994 by Jin et al.⁸ The very name of the phenomenon originates from the observation of the thousand fold change in the resistivity of the LCMO films near 77 K in the presence of applied magnetic field of 5 T. The material was epitaxial films of $\text{La}_{0.67}\text{Ca}_{0.33}\text{MnO}_3$ grown on LaAlO_3 substrates by laser ablation process. These manganites exhibit various ground states depending on the cation doping. Based on magnetization and resistivity, the inferred phase diagram of $\text{La}_{1-x}\text{Ca}_x\text{MnO}_3$, feature a number of distinct phases as shown in Fig. 1.^{9,10} The important electrons are the Mn d electrons, of which there is $4-x$ in these compounds

per formula unit. Changing the carrier concentration produces a variety of phases, which may be characterized by their magnetic, transport and charge-ordering properties.

At $x = 0$, the material is insulating at all temperatures but below 140 K it goes to antiferromagnetic phase. In fact the ground state remains insulating for $x \leq 0.2$ but the magnetic order changes in a complicated and still controversial way. This sequence of phases is denoted by canted anti-ferromagnetic and ferromagnetic insulator. One also sees that charge order develops inside the ferromagnetic insulator phase which is a periodic pattern of Mn sites in different valence states. Around $x = 0.2$, ground state changes from insulating to metallic. For $0.2 \leq x \leq 0.5$, ground state is ferromagnetic and then for $x \geq 0.5$, the ground state again becomes insulating and antiferromagnetic, and is in addition charge ordered. For a broad range of doping, these materials have a paramagnetic insulator to ferromagnetic metallic transition upon cooling which is accompanied by a sharp drop in resistivity. Our sample $x = 0.33$, shows paramagnetic insulating to ferromagnetic metallic phase transition at $T_{M-I} \approx 260$ K. Magnetic transition temperature is raised in a magnetic field, and thus the system could be tuned between low and high conductivity phases by applying a magnetic field. This result is a colossal magneto-resistance near T_c which could be as much as 100 thousand percent in thin films as mentioned in studies on CMR by S. Jin. Ferromagnetic transitions are in general very sensitive to applied fields though the very existence of the metal-insulator transition along with magnetic ordering is surprising. The physical origin of CMR effects in manganites is however different from the magnetoresistive properties of Fe/Cr multilayers which was found earlier by Binasch and Baibich and named as giant magnetoresistance (GMR).^{11,12} Subsequent studies on physical origination of CMR properties in manganites by Millis et al revealed the existence of the electron-phonon coupling due to the presence of dynamic Jahn-Teller distortion in manganites.^{10,13} The inclusion of JT coupling term along with DE term in the Hamiltonian provided more accurate prediction of Curie temperature and more realistic estimation of resistivity around T_c .

II. EXPERIMENTAL PROCEDURES

Our study in this articles focuses on the optical properties of $\text{La}_{0.67}\text{Ca}_{0.33}\text{MnO}_3$ (LCMO) thin film on NdGaO_3 (NGO) substrate. Pulsed laser deposition (PLD) technique was used to deposit a film of $\text{La}_{0.67}\text{Ca}_{0.33}\text{MnO}_3$ of around 140 nm thickness on a substrates NdGaO_3

(NGO). The growth process involved directing high-power KrF excimer laser pulses into a vacuum chamber on a rotating target material creating a supersonic jet of particles (plume) normal to the target surface. A heated substrate in the path of this resultant plume collected the ejected particles leading to epitaxial film growth. The film was deposited at 820°C with the rate of 0.05 nm/s. At room temperature, the film has orthorhombic unit cell with lattice parameters written below and shown in Figure 2.¹⁴

$$\begin{aligned}
 a &= 5.454 \text{ \AA}; & b &= 5.468 \text{ \AA}; & c &= 7.704 \text{ \AA}; & \alpha &= \beta = \gamma = 90^\circ \\
 \text{Mn-O1} &= 1.95 \text{ \AA}; & \text{Mn-O2} &= 1.96 \text{ \AA}; \\
 \text{Mn-O1-Mn} &= 159.9^\circ; & \text{Mn-O2-Mn} &= 161.0^\circ
 \end{aligned}$$

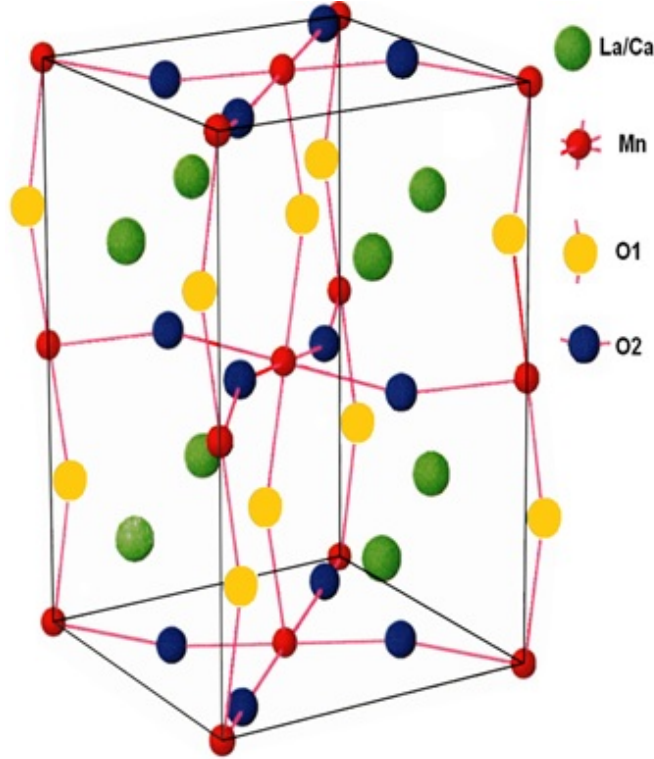


FIG. 2. (Color online) Orthorhombic crystal structure of $\text{La}_{0.67}\text{Ca}_{0.33}\text{MnO}_3$ thin film¹⁴. Reprinted figure with permission from Dai, P. and Zhang, Jiandi and Mook, H. A. and Liou, S. -H. and Dowben, P. A. and Plummer, E. W., Phys. Rev. B **54**, R3694(R) (1996). Copyright 1996 by the American Physical Society.

It has two different oxygen sites labelled as O1 and O2. In MnO_6 octahedral unit, four oxygen atoms forming the square in the horizontal plane are of one kind (O1 site) whereas one above and one below this square plane is of the second kind (O2 site). This octahedral

unit plays an important role in the course of phase transition and in the determination of other electronic and transport properties of this class of materials. The substrate NGO also has orthorhombic crystal structure with lattice parameters very close to the manganite film. The lattice parameters are given as¹⁵

$$a=5.428 \text{ \AA}; \quad b=5.498 \text{ \AA}; \quad c=7.709 \text{ \AA}; \quad \alpha = \beta = \gamma = 90^\circ$$

Since the lattice constants are well matched, there is negligible lattice strain (less than 0.1%), so makes it ideal to grow high quality thin and homogeneous films. It further allowed us to safely ignore any strain related issues in the analysis of the measured data.¹⁶ Temperature dependent (20 K–300 K) reflectance measurements were conducted on both the film and substrate over a frequency range of 30–20000 cm^{-1} . Measurements in far infrared and mid infrared region were conducted using a Bruker 113v Fourier Transform Infrared spectrometer. A helium-cooled silicon bolometer detector was used in the 40–650 cm^{-1} spectral range and a DTGS detector was used from 600–7000 cm^{-1} . Measurements in the near infrared and visible range were performed using a modified Perkin Elmer 16U grating spectrometer in conjunction with a continuous He flow cryostat. The spectrometer consists of different source of incident radiation and a suitable detector for the detection of the reflected radiation to cover the entire range. Room temperature reflectance data is extended up to 40,000 cm^{-1} for the better understanding of high frequency behavior for both the substrate and the manganite film. All optical measurements were performed using non-polarized light at near-normal incidence geometry on the epitaxial grown film with exposed (001) plane.

III. EXPERIMENTAL RESULTS AND ANALYSIS

The temperature dependence of the reflectance of $\text{La}_{0.67}\text{Ca}_{0.33}\text{MnO}_3$ thin film on NdGaO_3 thick substrate is shown in Fig. 3 between 30 and 20,000 cm^{-1} (3.7 meV–2.5 eV). In order to extract optical properties of $\text{La}_{0.67}\text{Ca}_{0.33}\text{MnO}_3$ only out of these spectra, we also need to know the contribution of NGO substrate. It leads us to measure the temperature dependent reflectance spectra of the substrate which is shown in Fig. 4.

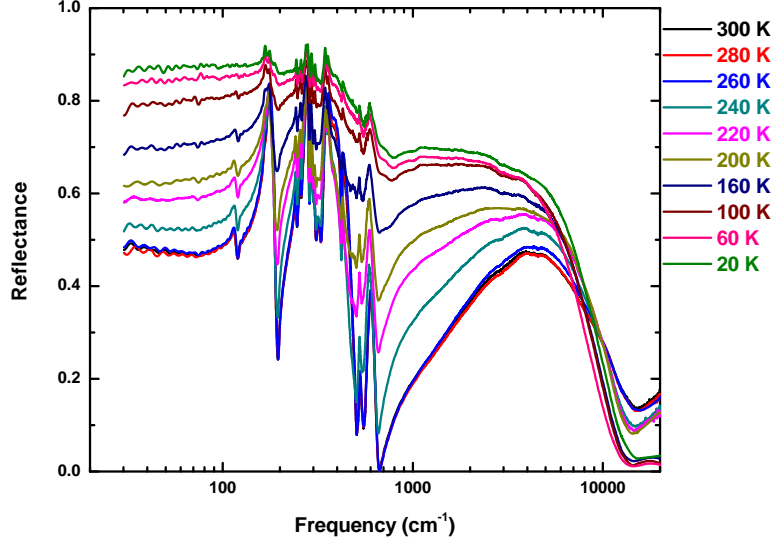


FIG. 3. (Color online) Temperature dependent reflectance spectra of $\text{La}_{0.67}\text{Ca}_{0.33}\text{MnO}_3$ thin film on a thick NGO substrate.

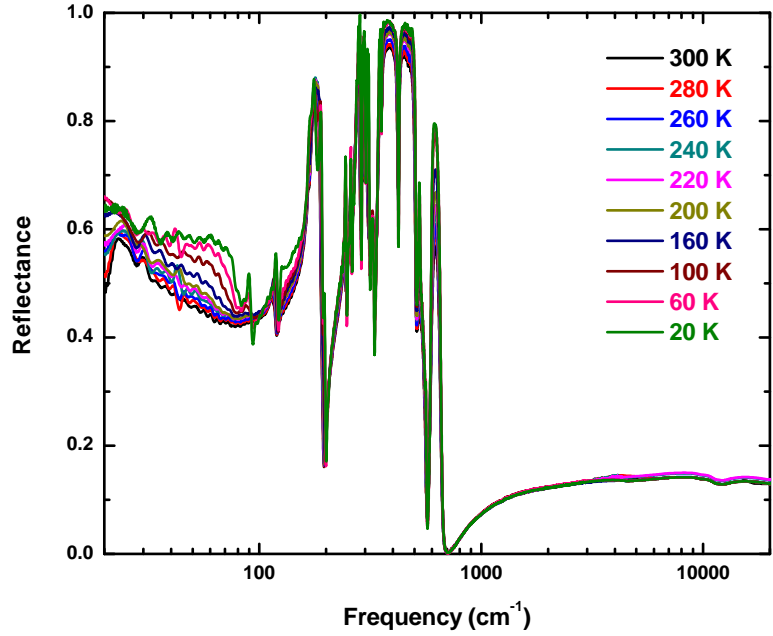


FIG. 4. (Color online) Temperature dependent reflectance spectra of a thick NdGaO_3 substrate.

In Fig. 4, the substrate reflectance does not show strong temperature dependence. The far-IR region is dominated by infrared active phonons at all temperatures. These phonon modes have also been reported and studied previously as a substrate for high- T_c superconductive films.^{17,18} A reststrahlen band is also seen between 300–500 cm^{-1} which becomes more pronounced as the temperature is lowered. The substrate becomes transparent above the

plasma minimum, at around 700 cm^{-1} . Beyond plasma minimum, substrate reflectance shows negligible frequency dependence, except around $11,500\text{ cm}^{-1}$ which is also previously reported.¹⁹ In Fig. 3, reflectance data of LCMO film on NGO substrate shows strong temperature dependence in all frequency regions except there is almost no change in measured reflectance between 260 K–300 K. We also see some of the substrate reflectance features around 100 cm^{-1} and 800 cm^{-1} . In infrared region, reflectance increases as temperature is decreased while in the visible region, reflectance increases as temperature is increased. Infrared region is dominated by phonons and strong phonon modes could be seen around 167 cm^{-1} , 340 cm^{-1} and 570 cm^{-1} . We also observe two weak modes around 385 cm^{-1} and 520 cm^{-1} . The visible region reflectance indicates a broad electronic transition mode or overlapping modes around $5000\text{--}8000\text{ cm}^{-1}$. Room temperature reflectance spectra up to $40,000\text{ cm}^{-1}$ is shown in Fig. 5 for both the thick substrate NGO and LCMO thin film on thick NGO substrate. High frequency spectra shows more interband transitions for both the substrate and the film.

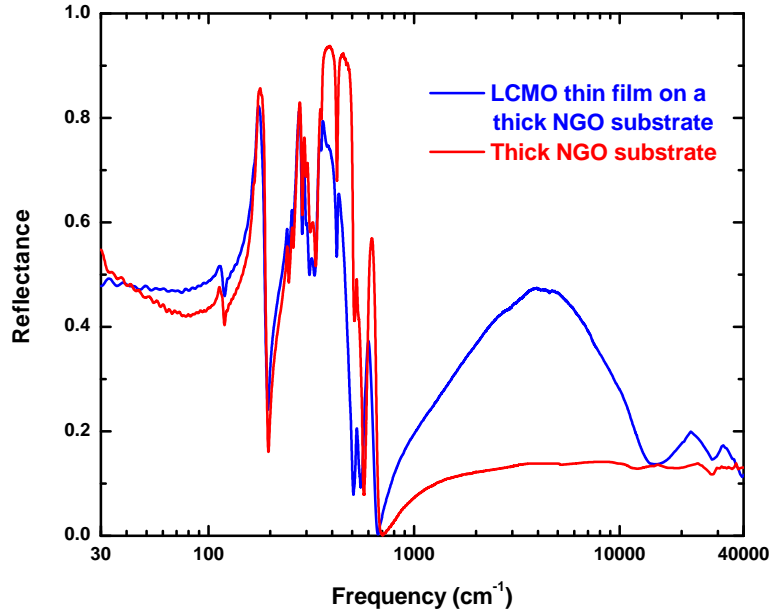


FIG. 5. (Color online) Room temperature reflectance spectra of LCMO thin film on NGO substrate and NGO substrate.

We performed Drude-Lorentz analysis on both the substrate and the film on substrate reflectance in order to derive other optical properties. The DL dielectric function is given as:

$$\varepsilon(\omega) = \varepsilon_{\infty} - \frac{\omega_p^2}{\omega^2 + i\omega/\tau} + \sum_{j=1}^N \frac{\omega_{pj}^2}{\omega_j^2 - \omega^2 - i\omega\gamma_j} \quad (1)$$

where the first term represents the core electron contribution (transitions above the measured range, the second term is free carrier contribution characterized by Drude plasma frequency ω_p and free carrier relaxation time τ and the third term is the sum of several Lorentzian oscillators representing phonons, and interband electronic contributions. The Lorentzian parameters are the j th oscillator plasma frequency ω_{pj} , its central frequency ω_j , and its linewidth γ_j . This dielectric function model is used in a least-squares fit to the reflectance. Table 1 shows the fitting parameters for substrate and the film at base temperature of 20 K and room temperature of 300 K.

| Symbol | NGO substrate (20 K) (cm ⁻¹) | NGO substrate (300 K) (cm ⁻¹) | LCMO film on NGO (20 K) (cm ⁻¹) | LCMO film on NGO (300 K) (cm ⁻¹) |
|---------------|--|---|---|--|
| ω_{p0} | | | 6980 | 370 |
| $1/\tau$ | | | 170 | 289 |
| ω_{p1} | 317 | 146 | 2670 | 780 |
| ω_1 | 61 | 30 | 165 | 170 |
| γ_1 | 47 | 36 | 60 | 65 |
| ω_{p2} | 46 | 171 | 1200 | 2600 |
| ω_2 | 90 | 70 | 340 | 330 |
| γ_2 | 2 | 66 | 10 | 200 |
| ω_{p3} | 61 | 83 | 450 | 200 |
| ω_3 | 119 | 116 | 520 | 380 |
| γ_3 | 2 | 7 | 10 | 15 |
| ω_{p4} | 489 | 393 | 630 | 250 |
| ω_4 | 170 | 173 | 562 | 520 |
| γ_4 | 9 | 5 | 15 | 30 |

| | | | | |
|----------------|-----|-----|--------|--------|
| ω_{p5} | 110 | 87 | 18,750 | 900 |
| ω_5 | 185 | 175 | 720 | 575 |
| γ_5 | 4 | 3 | 4470 | 110 |
| ω_{p6} | 227 | 114 | 7100 | 4000 |
| ω_6 | 245 | 243 | 1500 | 7600 |
| γ_6 | 2 | 3 | 2500 | 1220 |
| ω_{p7} | 236 | 97 | 6200 | 25,100 |
| ω_7 | 259 | 256 | 17,300 | 8800 |
| γ_7 | 2 | 2 | 7500 | 10,000 |
| ω_{p8} | 643 | 562 | | |
| ω_8 | 275 | 275 | | |
| γ_8 | 2 | 6 | | |
| ω_{p9} | 326 | 322 | | |
| ω_9 | 291 | 290 | | |
| γ_9 | 2 | 6 | | |
| ω_{p10} | 178 | 257 | | |
| ω_{10} | 304 | 300 | | |
| γ_{10} | 3 | 10 | | |
| ω_{p11} | 247 | 388 | | |
| ω_{11} | 321 | 319 | | |
| γ_{11} | 9 | 21 | | |
| ω_{p12} | 528 | 546 | | |
| ω_{12} | 343 | 345 | | |
| γ_{12} | 4 | 11 | | |
| ω_{p13} | 185 | 266 | | |
| ω_{13} | 356 | 356 | | |

| | | | | |
|----------------|-------|-------|--|--|
| γ_{13} | 2 | 7 | | |
| ω_{p14} | 136 | 151 | | |
| ω_{14} | 425 | 424 | | |
| γ_{14} | 5 | 9 | | |
| ω_{p15} | 97 | 107 | | |
| ω_{15} | 516 | 516 | | |
| γ_{15} | 11 | 16 | | |
| ω_{p16} | 131 | 113 | | |
| ω_{16} | 547 | 539 | | |
| γ_{16} | 33 | 30 | | |
| ω_{p17} | 227 | 259 | | |
| ω_{17} | 591 | 592 | | |
| γ_{17} | 11 | 27 | | |
| ω_{p18} | 2766 | 2425 | | |
| ω_{18} | 10695 | 10318 | | |
| γ_{18} | 3140 | 3155 | | |

TABLE I: Drude-Lorentz parameters for NGO substrate and LCMO film on substrate at 20 K and 300 K.

Figure 6 shows the fit to the reflectance spectra of LCMO film on substrate at the base temperature of 20 K and at room temperature of 300 K. Firstly the substrate reflectance data was fitted using Drude-Lorentz model and later knowing the dielectric function of substrate, one can extract the dielectric function of the LCMO film. The relevant equations for thin film analysis is given as:

$$R_s(\omega) = \left| \frac{\sqrt{\varepsilon_s(\omega)} - 1}{\sqrt{\varepsilon_s(\omega)} + 1} \right|^2 \quad (2a)$$

$$R_f(\omega) \approx R_{af}(\omega) + [1 - R_{af}(\omega)]^2 R_{fs}(\omega) e^{-2\alpha_f(\omega)d} \quad (2b)$$

Here R_s , R_f and R_{af} are reflectance of substrate, reflectance of film and prompt reflectance from air-film interface. Note here that R_s and R_f are measured experimentally and R_{af} is derived using the above formula. In addition, d is the thickness of the film and $\alpha_f(\omega)$ is dependent on R_{af} indirectly.

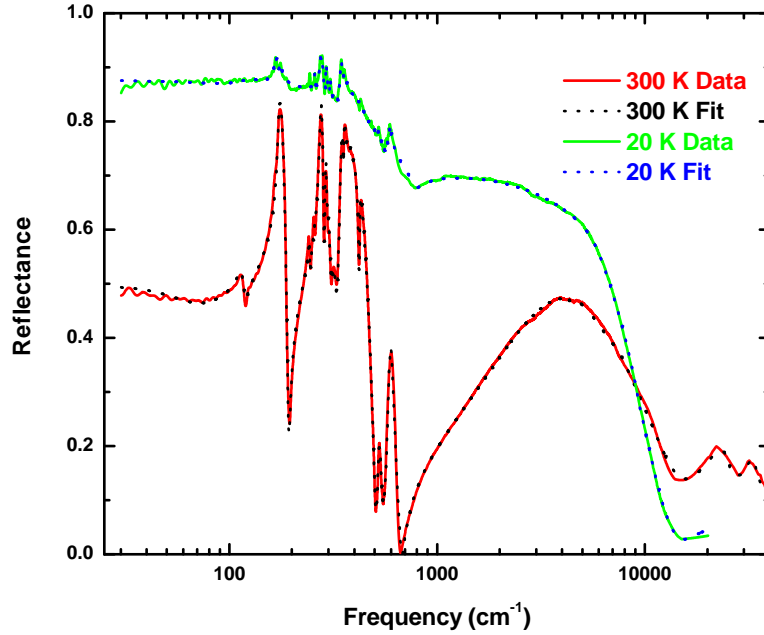


FIG. 6. (Color online) Drude-Lorentz fit to the room temperature and base temperature reflectance spectra of LCMO thin film on NGO substrate.

Fitting procedure is repeated at all other temperatures in order to analyze the temperature dependence of these parameters which will be discussed later. Once the Drude-Lorentz parameters are found for substrate and film, other optical properties could be calculated. Fig. 7 and 8 shows the real part of the optical conductivity for the substrate and film respectively.

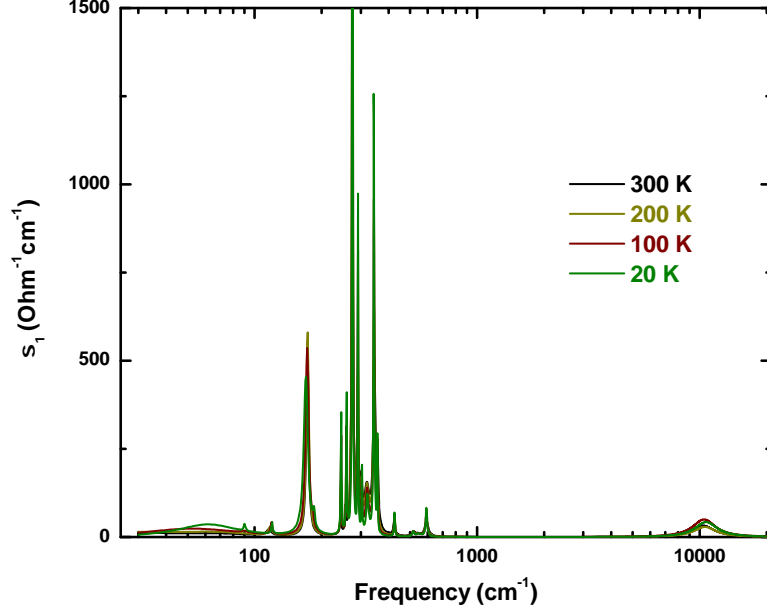


FIG. 7. (Color online) Drude-Lorentz parameter calculated real part of optical conductivity of NGO substrate at several temperatures.

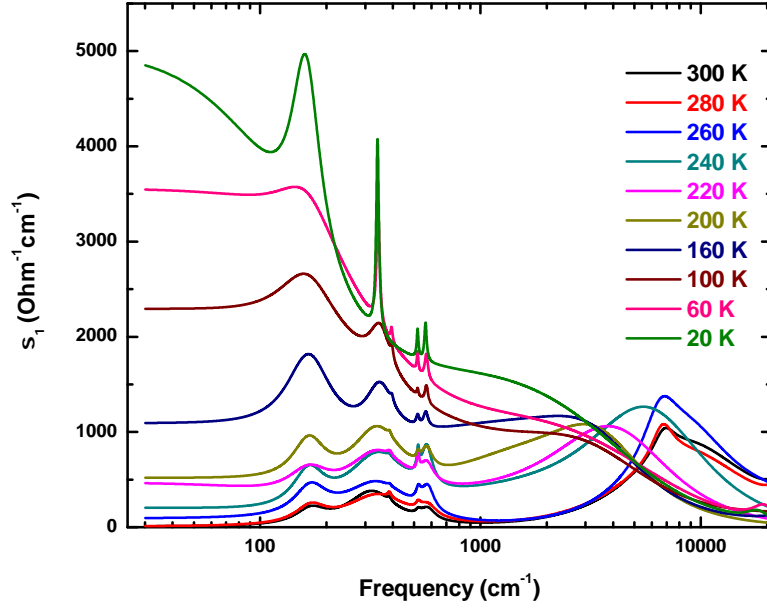


FIG. 8. (Color online) Temperature dependence of real part of optical conductivity of LCMO thin film calculated using Drude-Lorentz parameters.

As we can see that substrate is an insulator and shows all Far-infrared phonon modes. There is no temperature dependence observed in the calculated conductivity spectra, as expected from a weakly temperature dependent spectra shown in Figure 4. However LCMO film conductivity plot shows strong temperature dependence in all frequency regions. In the

film, a systematic increase is seen both in the Drude component and the mid-IR component of the conductivity. This is expected as the system goes to its low temperature ferromagnetic metallic ground state. The large asymmetric mid-IR band in the film has been interpreted as due to large lattice polarons²⁰ following the theoretical investigations of Emin et al.²¹ According to the theory, a coherent band of the large polaron should show up only at lower frequencies below characteristic phonon modes and become more significant as T decreases. In addition, its photo-ionization should bring out an incoherent mid-IR band which is very asymmetric and shows a long tail above its peak position. Thus the Drude component was attributed to a coherent motion of a large polaron, and the mid IR band was attributed to its incoherent absorption band. In Far and mid infrared region as we cool down the sample, we observe large increase in the conductivity. The Drude component decreases rapidly as temperature increases and almost vanishes around 240–260 K range. We see strong peaks at 167, 340 and 570 cm^{-1} and two weak modes around 385 and 520 cm^{-1} same as in reflectance plot. In visible region, as we cool down the sample, conductivity decreases and forms a shallow minimum at low temperature. At room temperature, at least two strong, wide and overlapping peaks in the range of 6000–8000 cm^{-1} is observed, which is common in hole doped manganites representing manganese e_g - e_g states transitions within the parallel spin manifold. These transitions appears to shift to the lower frequency and their strengths shows strong temperature dependence which will be discussed next.

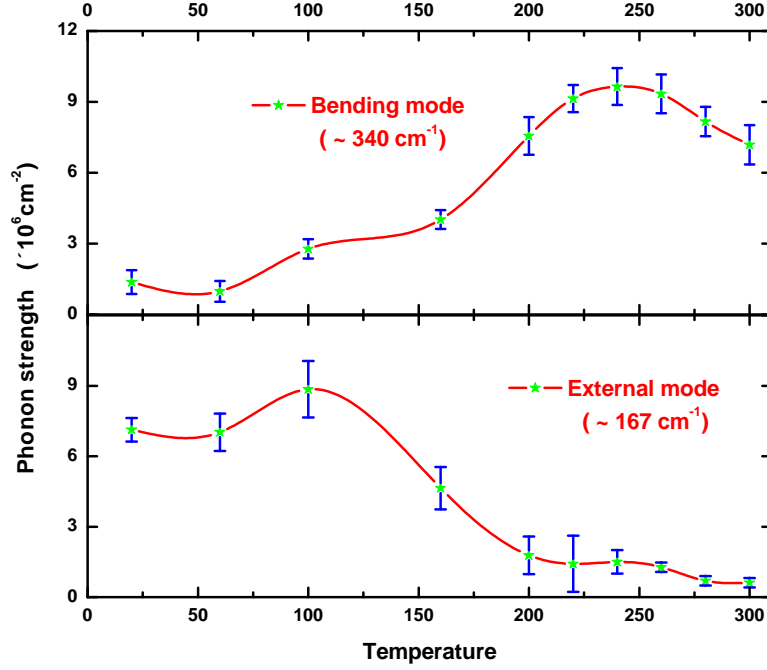


FIG. 9. (Color online) Temperature dependence of phonon strength of external mode and bending mode in LCMO film.

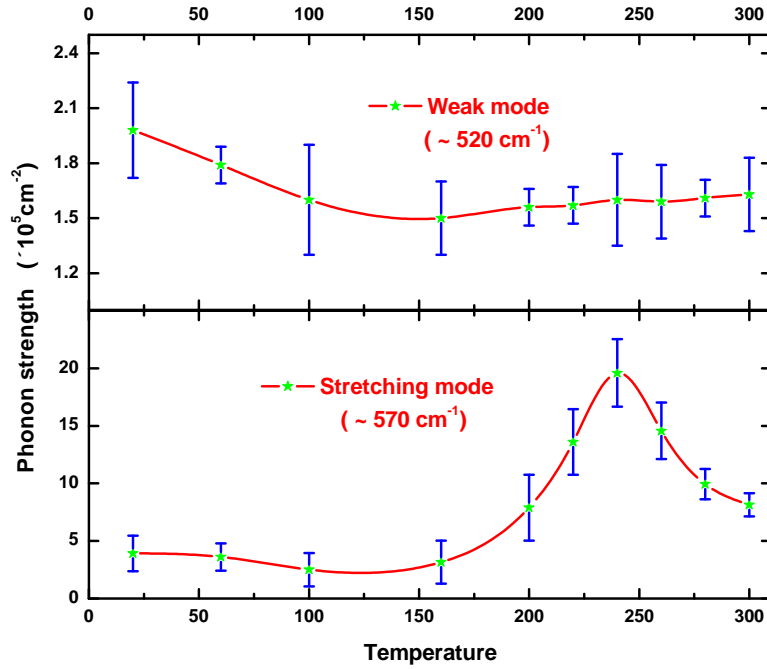


FIG. 10. (Color online) Temperature dependence of phonon strength of stretching mode and another weak mode in LCMO film.

Temperature dependence of oscillator strength of important phonon modes are shown in figure 9 and 10. The external mode at 167 cm^{-1} represents a vibrating motion of the

divalent or trivalent cations against MnO_6 octahedral unit shows maximum strength around 100 K and then it decreases as you increase the temperature. The bending mode at 340 cm^{-1} which reflects an internal motion of the Manganese and Oxygen ions located along a particular direction against the other Oxygen ions in a plane perpendicular to it, shows an increase in strength with temperature and passes through a weak maxima around 240–260 K. On the other hand, the stretching mode at 570 cm^{-1} which corresponds to an internal motion of the Manganese ion against the Oxygen octahedron shows increase in strength with temperature and has a maxima around critical temperature of 240–260 K. Another weak mode at 520 cm^{-1} doesn't show much temperature dependence.

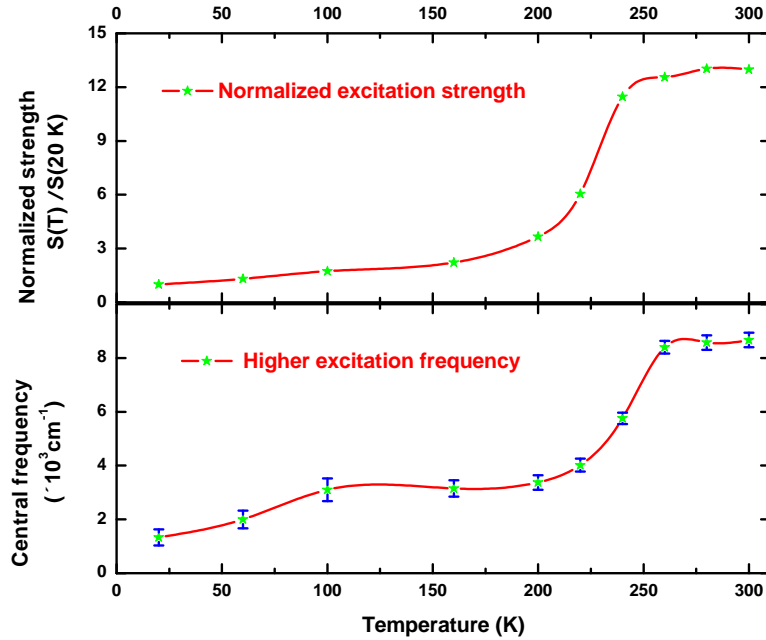


FIG. 11. (Color online) Temperature dependence of excitation frequency and excitation strength of higher electronic transition in LCMO film.

Temperature dependence of other parameters related to the electronic excitations in the visible range is shown in figure 11. The basic building block of the manganites are the MnO_6 octahedra. Each manganese is in a locally cubic environment and the hybridization and electrostatic interaction with oxygen 2p electron will cause crystal field splitting of degenerate 5 d-orbitals into lower lying t_{2g} triplet and higher e_g doublet. The triplet levels seems to lie substantially below the doublet level, around 2-4 eV. In Mn^{3+} ions, 3 out of 4 electrons stay in t_{2g} triplet states and fourth electron stay in one of the e_g doublet state. On the other hand in Mn^{4+} ions, all 3 electrons stay in t_{2g} triplet states and e_g doublet

states are empty. Above the critical temperature of around 240–260 K, the remaining degeneracy of 3d orbitals are broken due to lattice motion. The oxygen ions surrounding the Mn^{3+} ions can slightly readjust their locations, creating an asymmetry between different directions that effectively removes the degeneracy. This lifting of degeneracy due to orbital-lattice interaction is called Jahn-Teller effect. Mn^{4+} ions do not have any electron in e_g level, therefore there is no JT splitting there. This high temperature insulating phase with significant JT distortion creates an energy gap between e_g doublet states. In LaMnO_3 , this gap is reported between 1–2 eV.^{1,22,23} Besides, these states have wide energy spread of about 1 eV due to unstable and non-uniform JT distortion.² The electronic transition in figure 11 represents the excitation of the electron in e_g^1 state below the Fermi level to e_g^2 state above the Fermi level. The transition frequency and transition strength decrease as temperature decreases up to 240–260 K and then there is a sharp drop in transition frequency and oscillator strength. This behavior suggests that material goes into low temperature ferromagnetic and metallic phase with minimum JT distortion. It leads to a decrease in the JT splitting energy as well as decrease in the density of states, explaining the decreases in the transition frequency and decreasing strength. This also indicates that the spectral weight shifts to the lower frequency as temperature goes down.

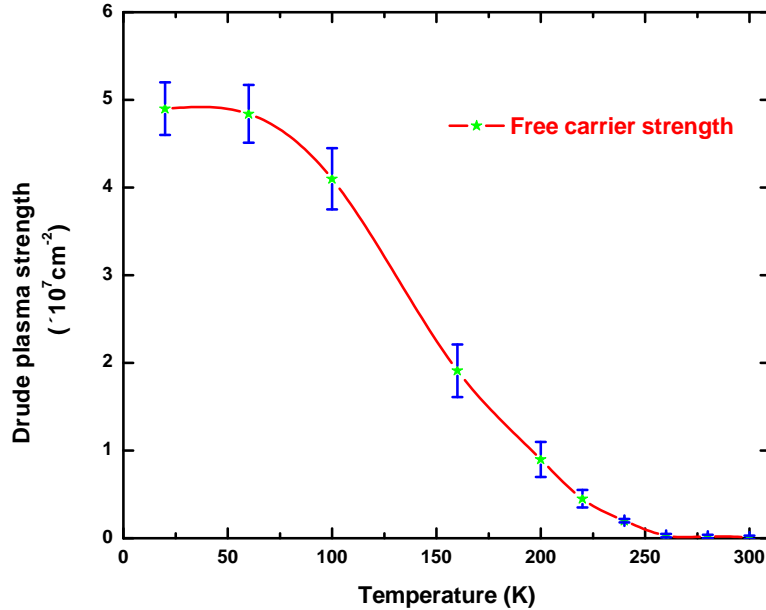


FIG. 12. (Color online) Temperature dependence of Drude plasma strength in LCMO film.

Figure 12 shows the temperature dependence of free carrier strength. Drude strength goes

to almost zero around 240–260 K suggesting the transition from low temperature metallic phase to high temperature insulating phase. The Drude component has more or less temperature independent scattering rate in the measurement range and Drude conductivity has no role in mid-infrared range. A strong electron-phonon coupling at high temperature may localize carriers, because the presence of an electron in a given Mn orbital causes a local lattice distortion which produces a potential minimum, which tends to trap the electron in that orbital. If the coupling is strong enough, these tendencies lead to the formation of a self-trapped state called a polaron. This self trapping competes with the delocalizing tendency of electron hybridization. In high temperature phase, the electron-phonon interaction localizes the electron causing insulating phase whereas as T decreases, the delocalization tendency of e_g electrons becomes stronger and metallic character prevails.

IV. CONCLUSIONS

Temperature dependent reflectance measurement shows very weak temperature dependence for NGO substrate whereas LCMO film shows strong temperature dependence. The Drude-Lorentz analysis allowed to calculate temperature dependent conductivity spectra which also shows strong temperature dependence. Strong phonon modes at 167, 340 and 570 cm^{-1} were identified as external mode, bending mode and stretching mode. These phonons have strong temperature dependent oscillator strength and some of these oscillators show maximum strength around 240–260 K. The Drude conductivity component almost vanishes above 240–260 K. Free carriers do not show much variation in scattering rate with temperature. In the visible region, there is a wide, strong and overlapping electronic transition mode around 8000 cm^{-1} in the high temperature insulating phase which shifts gradually to lower frequency with a reduced strength as temperature decreases and then there is a sharp drop in transition frequency and strength around 240–260 K suggesting a phase transformation. It turns out that below 240–260 K, LCMO goes into metallic phase with ferromagnetic moment ordering. This characteristic behavioral change in electrical and magnetic properties is due to strong electron-phonon coupling in manganites also known as Jahn-Teller coupling. For Ca doped manganite film with stoichiometry $\text{La}_{0.67}\text{Ca}_{0.33}\text{MnO}_3$, there exist a ferromagnetic

metal to paramagnetic insulator phase transition around 240–260 K.

- * Senior Test Engineer, Areva Solar, 2585 E Bayshore Rd, Palo Alto, CA 94303
- † Department of Physics, Pusan National University, Busan, South Korea
- ¹ J. H. Jung, K. H. Kim, T. W. Noh, E. J. Choi, and J. Yu, Phys. Rev. B **57**, R11043 (1998).
- ² S. Satpathy, Z. S. Popovi, and F. R. Vukajlovi, Journal of Applied Physics **79**, 4555 (1996).
- ³ G. Jonker and J. V. Santen, Physica **16**, 337 (1950).
- ⁴ J. H. V. Santen and G. H. Jonker, Physica **16**, 599 (1950).
- ⁵ C. Zener, Phys. Rev. **82**, 403 (1951).
- ⁶ E. O. Wollan and W. C. Koehler, Phys. Rev. **100**, 545 (1955).
- ⁷ Q. Huang, A. Santoro, J. W. Lynn, R. W. Erwin, J. A. Borchers, J. L. Peng, and R. L. Greene, Phys. Rev. B **55**, 14987 (1997).
- ⁸ S. Jin, T. H. Tiefel, M. McCormack, R. A. Fastnacht, R. Ramesh, and L. H. Chen, Science **264**, 413 (1994), <http://www.sciencemag.org/content/264/5157/413.full.pdf>.
- ⁹ P. Schiffer, A. P. Ramirez, W. Bao, and S.-W. Cheong, Phys. Rev. Lett. **75**, 3336 (1995).
- ¹⁰ A. J. Millis, Nature **392**, 147 (1998).
- ¹¹ G. Binasch, P. Grünberg, F. Saurenbach, and W. Zinn, Phys. Rev. B **39**, 4828 (1989).
- ¹² M. N. Baibich, J. M. Broto, A. Fert, F. N. Van Dau, F. Petroff, P. Etienne, G. Creuzet, A. Friederich, and J. Chazelas, Phys. Rev. Lett. **61**, 2472 (1988).
- ¹³ A. J. Millis, P. B. Littlewood, and B. I. Shraiman, Phys. Rev. Lett. **74**, 5144 (1995).
- ¹⁴ P. Dai, J. Zhang, H. A. Mook, S. H. Liou, P. A. Dowben, and E. W. Plummer, Phys. Rev. B **54**, R3694 (1996).
- ¹⁵ M. Schmidbauer, A. Kwasniewski, and J. Schwarzkopf, Acta Crystallographica Section B **68**, 8 (2012).
- ¹⁶ T. Wu, S. B. Ogale, S. R. Shinde, A. Biswas, T. Polletto, R. L. Greene, T. Venkatesan, and A. J. Millis, Journal of Applied Physics **93**, 5507 (2003).
- ¹⁷ P. Calvani, M. Capizzi, F. Donato, P. Dore, S. Lupi, P. Maselli, and C. Varsamis, Physica C: Superconductivity **181**, 289 (1991).
- ¹⁸ Z. M. Zhang, B. I. Choi, M. I. Flik, and A. C. Anderson, J. Opt. Soc. Am. B **11**, 2252 (1994).

- ¹⁹ V. M. Orera, L. E. Trinkler, R. I. Merino, and A. Larrea, *Journal of Physics: Condensed Matter* **7**, 9657 (1995).
- ²⁰ K. H. Kim, J. H. Jung, and T. W. Noh, *Phys. Rev. Lett.* **81**, 1517 (1998).
- ²¹ D. Emin, *Phys. Rev. B* **48**, 13691 (1993).
- ²² T. Arima, Y. Tokura, and J. B. Torrance, *Phys. Rev. B* **48**, 17006 (1993).
- ²³ T. Saitoh, A. E. Bocquet, T. Mizokawa, H. Namatame, A. Fujimori, M. Abbate, Y. Takeda, and M. Takano, *Phys. Rev. B* **51**, 13942 (1995).